Dynamical analysis of the upwelling circulation off central Chile

Jorge M. Mesias,[1] Ricardo P. Matano, and P. Ted Strub
College of Oceanic and Atmospheric Sciences, Oregon State University, Corvallis, Oregon, USA

Received 4 September 2001; revised 16 May 2002; accepted 13 December 2002; published 18 March 2003.

[1] In this article we analyze the momentum and vorticity balances of a numerical simulation of the upwelling circulation off central Chile (34°–40°S) and its response to interannual local wind changes. Our analysis indicates that the path of the upwelling jet is strongly controlled by the bottom topography. This topographic steering causes the jet to separate from the coast at the Punta Lavapie cape (∼37°S). Although the zeroth-order momentum balance is dominated by the geostrophic terms, the circulation is also affected by nonlinear processes, which lead to the formation of large meanders and the shedding of cyclonic eddies north of Punta Lavapie during periods of wind relaxation. The relative contributions of the zeroth-order vorticity balance and the advective terms are also strongly controlled by changes in the coastline geometry and the bottom topography. Vorticity is created along the current axes and transported toward the coast and the Peru-Chile Trench, where it dissipates. South of Punta Lavapie the across-shelf transports are weaker with equatorward flows that are more stable than in the north. Additional numerical simulations indicate that during periods with El Niño conditions, the area is affected with a general weakening of the currents and upwelling activity, although the northern region still shows the formation of eddies. During years with relatively stronger winds, in contrast, the upwelling activity and across-shelf transport processes are significantly increased. The results show that the Punta Lavapie cape has a large effect on the spatial and temporal variability of the coastal currents in the region off central Chile. *INDEX TERMS:* 4279 Oceanography: General: Upwelling and convergences; 4255 Oceanography: General: Numerical modeling; 4520 Oceanography: Physical: Eddies and mesoscale processes; 4522 Oceanography: Physical: El Niño; *KEYWORDS:* upwelling dynamics, vorticity, eddies, numerical modeling, central Chile, El Niño

Citation: Mesias, J. M., R. P. Matano, and P. T. Strub, Dynamical analysis of the upwelling circulation off central Chile, *J. Geophys. Res.*, *108*(C3), 3085, doi:10.1029/2001JC001135, 2003.

1. Introduction

[2] In a previous article [*Mesias et al.*, 2001] (hereinafter referred to as M2001) the characteristics of the upwelling regime along the central region of the Chilean coast were described using a three-dimensional primitive equation model. The model was forced with wind stress fields from the European Center for Medium Weather Forecasts (ECMWF) during summer of 1993.

[3] Following the set-up of the upwelling regime [*Allen et al.*, 1995], our M2001 numerical experiment shows the development of an eastern boundary current system consisting of a strong surface equatorward jet and a deep poleward undercurrent. The circulation in the coastal region is dominated by an upwelling regime characterized by periods of growth and decay that follow the intensification and relaxation of the wind forcing.

[4] The results of M2001 also indicate that the upwelling circulation along the Chilean coast is strongly dependent on the bottom topography, coastline geometry and the local wind forcing. To quantify these effects, in this article we analyze the momentum and vorticity balance of the M2001 experiment. The goal is to elucidate the dynamical processes that lead to the separation of the equatorward jet from the coast and the subsequent eddy formation. We also study the response of the oceanic circulation to interannual changes in the magnitude of the wind forcing, to assess the effects of interannual atmospheric variations associated with El Niño Southern Oscillation (ENSO) events. To this effect, we analyze two additional numerical simulations forced with wind stress fields during the summers of years 1992 and 1994.

[5] This article is organized as follows. In section 2 we present a brief description of our experimental set-up. In section 3 we summarize the results from our previous benchmark experiment and analyze the momentum and vorticity balances. In section 4 we discuss the differences in the circulation caused by interannual changes in the wind forcing. Finally, in section 5 we present our summary and conclusions.

2. Experimental Set-Up

[6] The numerical experiments discussed in this article use the three-dimensional, primitive equation, Princeton

[1]Now at School for Marine Science and Technology, University of Massachusetts, Dartmouth, Massachusetts, USA.

0148-0227/03/2001JC001135$09.00

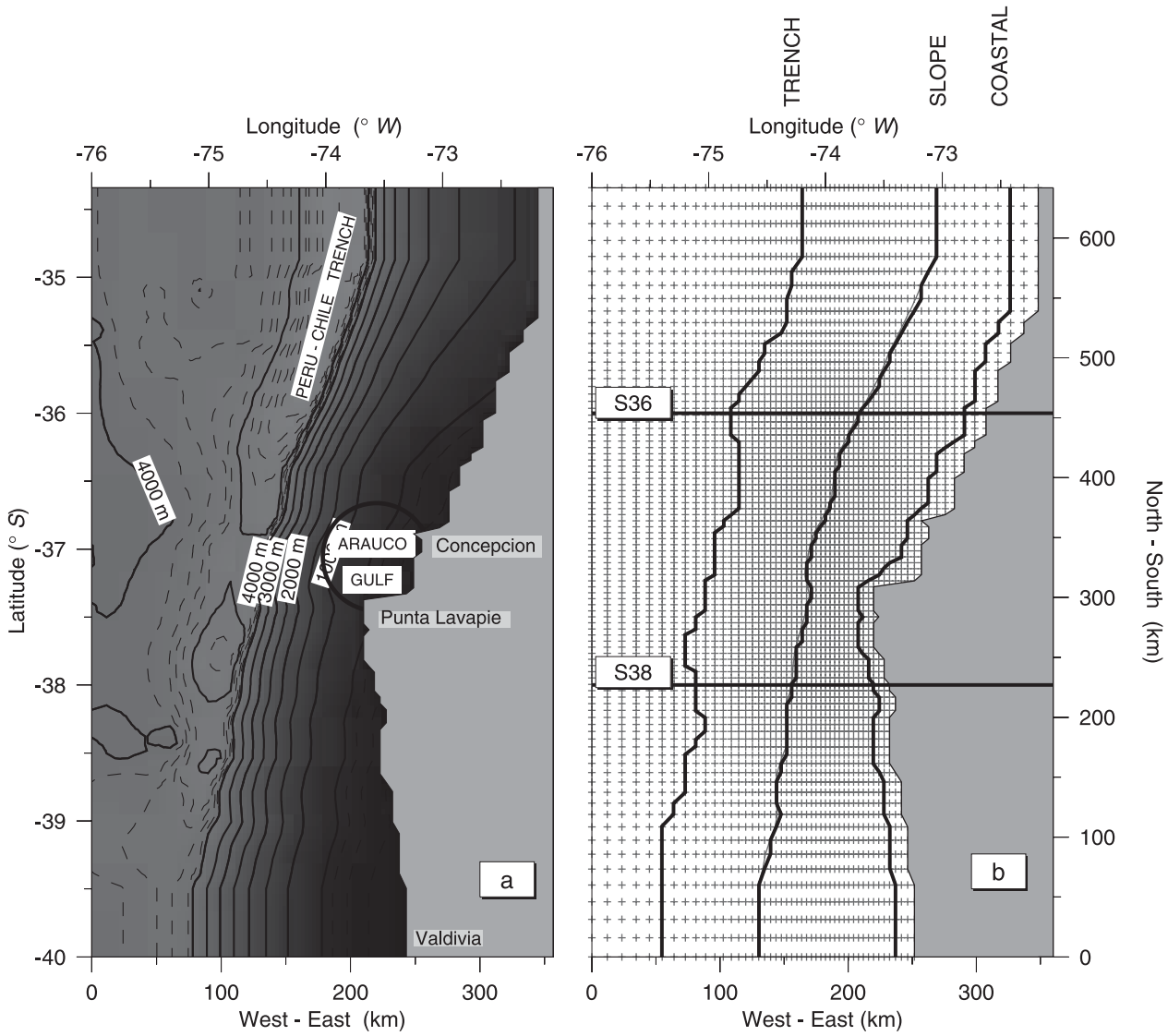

Figure 1. (a) Bottom topography (in meters) of the model domain. (b) Horizontal model grid (shaded pluses). Dark lines correspond to sections used for the analysis of the model outputs.

Ocean Model. The model includes a free surface and uses a sigma-coordinate transformation that scales the size of each vertical level to the water depth. The coefficients of horizontal mixing of the model are calculated using the scheme described by *Smagorinsky* [1963], while the coefficients of vertical mixing follow the second-order turbulence closure scheme described by *Mellor and Yamada* [1982]. A complete description of the model is given by *Blumberg and Mellor* [1987]. The model uses a split mode time step that solves the vertically integrated equations (external mode) separately from the vertical structure equations (where variables represent absolute fields, i.e., variables of the full three-dimensional set of momentum equations).

[7] The model domain and bottom relief representing the Gulf of Arauco region are shown in Figure 1. The horizontal grid spacing of the model ranges from 3.5 km near the coast to 13 km farther offshore, while the vertical axis is discretized using 15 sigma-levels with higher resolution in the upper layers. The model is initialized with summer climatological temperature and salinity values derived from the *Levitus and Gelfeld* [1992] monthly climatology, and forced at its surface with summer time ECMWF wind stresses [*Lonnberg et al.*, 1989] for years 1992, 1993 and 1994. The simulations of the summertime oceanic conditions were started from rest on January 1 and run for periods of 100 days for each year. The surface heat and salt fluxes are simulated through a relaxation of the temperature and salinity values at the uppermost level to the monthly climatological values of *Levitus and Gelfeld* [1992]. The relaxation scheme and the conditions implemented at the open boundaries of the model are fully described by M2001.

3. Dynamical Analysis

[8] For the sake of completeness, in this section we summarize the results described by M2001. Figure 2 shows the temporal evolution of the alongshore wind stress and

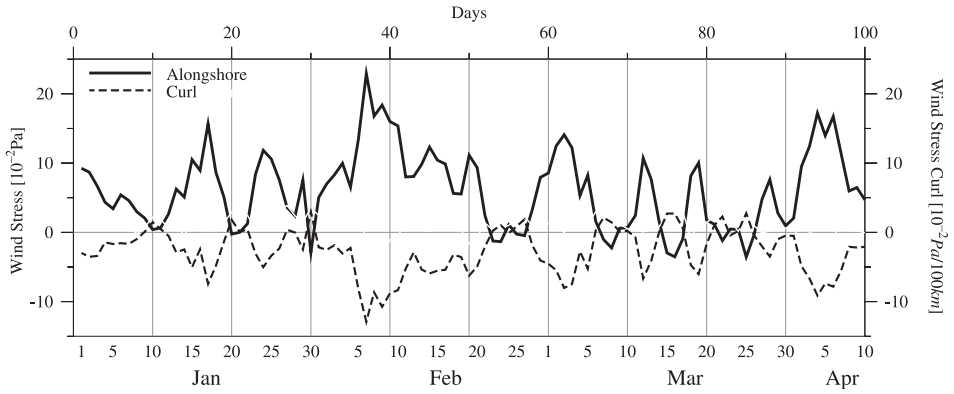

Figure 2. Evolution of area-averaged alongshore wind stress component and wind stress curl fields during the benchmark experiment for summer of 1993.

wind stress curl fields used to drive the model. The wind conditions during this time period are characterized by intense upwelling favorable conditions followed by short spans of relaxation.

[9] Figure 3 shows time-averaged (last 50 days of the numerical simulation) temperature and velocity fields of the benchmark experiment. The mean temperature field in Figure 3b shows the upwelling of cold waters along the coast as induced by the equatorward winds and negative (cyclonic) wind stress curl, which is enhanced at the Punta Lavapie cape (at ~37°S) [*Vergara*, 1993]. The velocity structure of the flow in Figures 3a, 3c, and 3d depict a current system that consist of a strong surface coastal jet, following the contours of the bottom relief (Figure 1a), and a weak poleward subsurface current, flowing at depths of 200–500 m, with absolute maxima of ~0.05 and ~0.10 m s^{-1} at 36 and 38°S, respectively. Our benchmark simulation also predicts a relatively strong subsurface equatorward current located over the upper continental slope at ~1000 m depth (Figures 3c and 3d).

[10] The M2001 results indicate that the general pattern of oceanic variability can be divided into two regions separated by the Punta Lavapie cape. To the south of Punta Lavapie, the circulation is dominated by a relatively stable equatorward jet flowing very close to the coast. To the north of Punta Lavapie (in the Gulf of Arauco region) the equatorward jet separates from the coast. During the periods of wind relaxation, the separated jet continues its northward movement while currents next to the coast become poleward, creating cyclonic eddies.

[11] Our model results, presented by M2001, suggest that there is a large degree of topographic steering, which is consistent with previous observations indicating that the region off central Chile is prone to highly geostrophic flows [*Strub et al.*, 1998]. In this context, the fact that the model poleward undercurrent was poorly (weak) reproduced could be explained in two ways: 1) The model does not have enough baroclinicity to overcome the relatively stronger barotropic pressure gradient related to the sloping sea surface, or 2) the existence and variability of the undercurrent off central Chile could be due to forcings of remote origins (at 36°S, there is low coherence between local winds and surface currents [*Mesias et al.*, 2001]), or to forcings that could be "determined" at larger (basin) spatial scales than those defined by our model settings. Although there are several other mechanisms that could explain the undercurrent dynamics [*Strub et al.*, 1998], their relative importance remains unknown and more studies are needed to reveal their individual or combined significance. Overall, however, comparisons between the variability of satellite-derived and model sea surface temperature fields (to be informed in a follow up to this paper) indicate that our model simulations have "captured" important components of the upwelling dynamics off central Chile. To gain further understanding into the dynamics of this upwelling regime, the following subsections analyze the momentum and vorticity balances of this benchmark experiment.

3.1. Momentum Balance

[12] The momentum balance equation can be written as

$$\alpha_t = \mathcal{F}, \tag{1}$$

where $\alpha_t = \frac{1}{D}\frac{\partial(\mathrm{v}D)}{\partial t}$ is the horizontal acceleration, and

$$\mathcal{F} = -[\mathbf{k}\times(f\mathrm{v})] - \left[\nabla(g\eta) + \frac{1}{D}\boldsymbol{\Phi}\right] - \left[\frac{1}{D}\mathcal{A}\right] - \left[\frac{1}{D}\mathcal{V}\right] \tag{2}$$

is the sum of the momentum terms identified below.

[13] In equation (2), $\boldsymbol{\Phi} \equiv \frac{gD}{\rho_0}\int_\sigma^0 \left[\nabla\rho - \sigma\nabla D\frac{\partial_\rho}{\partial_\sigma}\right]d\sigma$ represents the baroclinic part of the pressure gradient, $\mathcal{A} \equiv [\nabla\cdot(\mathbf{v}D) + \mathbf{v}D\cdot\nabla]\mathbf{v} - \mathbf{F}$ is the sum of the horizontal components of advection and viscosity, and $\mathcal{V} \equiv \frac{\partial}{\partial\sigma}\left(\omega\mathbf{v} - \frac{K_M}{D}\frac{\partial\mathbf{v}}{\partial\sigma}\right)$ represents the vertical components of advection and viscosity. The horizontal components of viscosity ($\mathbf{F}$) are given by $F_x \equiv \frac{\partial}{\partial x}(H\tau_{xx}) + \frac{\partial}{\partial y}(H\tau_{xy})$ and $F_y \equiv \frac{\partial}{\partial x}(H\tau_{xy}) + \frac{\partial}{\partial y}(H\tau_{yy})$, with stress terms $\tau_{xx} \equiv 2A_M\frac{\partial u}{\partial x}$, $\tau_{xy} = \tau_{yx} \equiv A_M\left(\frac{\partial u}{\partial y} + \frac{\partial v}{\partial x}\right)$, and $\tau_{yy} \equiv 2A_M\frac{\partial v}{\partial y}$. In the external mode, the vertical components of advection and viscosity becomes $\int_\sigma^0 \mathcal{V}d\sigma = \tau_0 - \tau_B$, i.e., the sum of the surface and bottom stresses. See the notation table to identify symbols not defined here. For farther explanations on the derivation of equation (2) and terms in the vertically integrated mode, see the paper by *Blumberg and Mellor* [1987].

[14] The (square bracketed) momentum terms in equation (2) are hereinafter identified as Coriolis, pressure gradient,

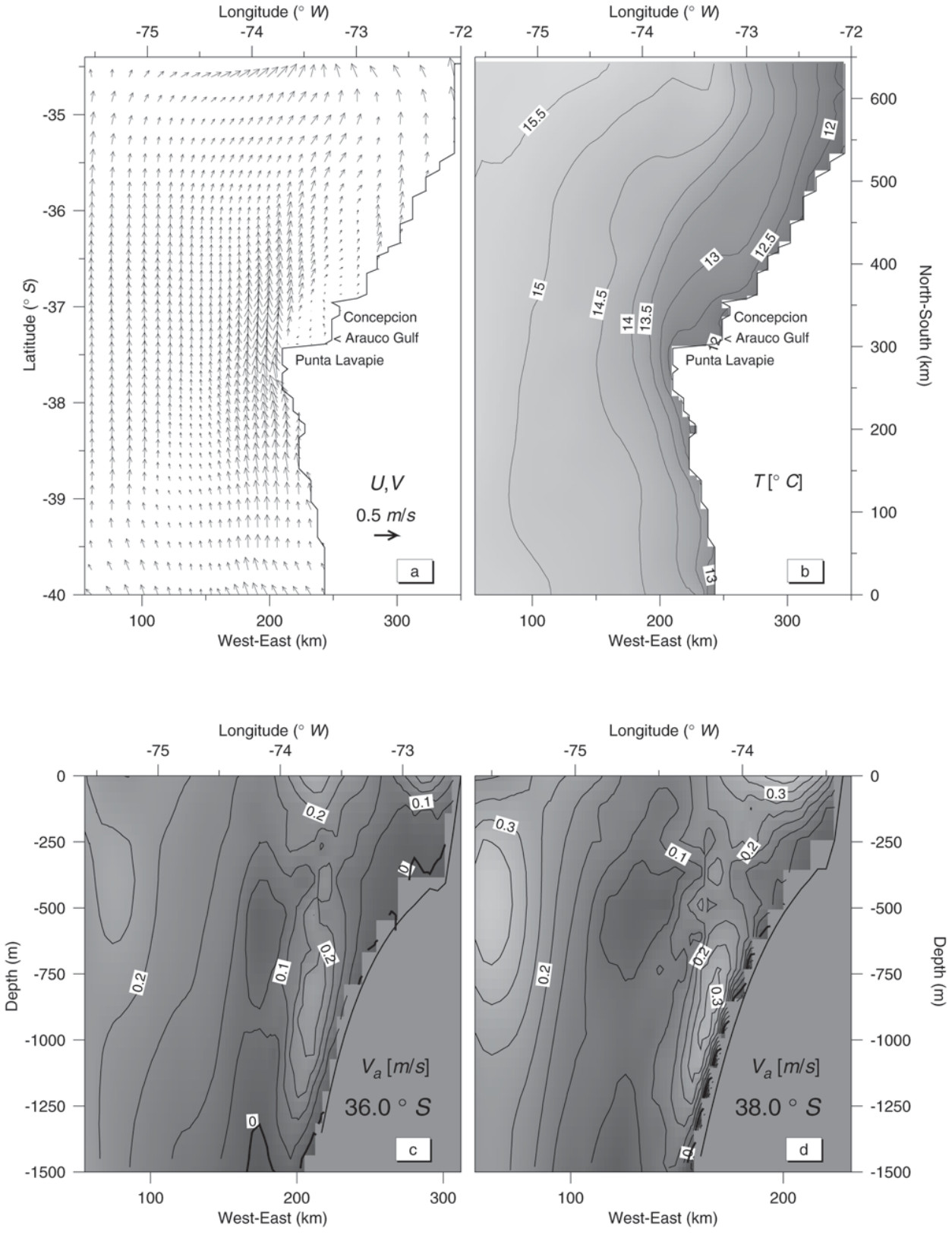

Figure 3. Maps of time-averaged (last 50 simulation days) model fields from the benchmark experiment. Depicted fields are (a) surface velocity, (b) surface temperature, and cross-shelf sections of alongshore currents at latitudes (c) 36°S and (d) 38°S. The contour interval is 0.05 m s^{-1}, and shading denotes poleward alongshore flows.

horizontal advection plus diffusion, and vertical advection plus diffusion (or surface stress plus bottom stress for the external mode). Since diffusion represents unresolved advection, we refer to horizontal advection plus diffusion also as the (nonlinear) inertial term.

[15] To analyze the model output we average the terms of equation (2) over regions of 50 km × 50 km, centered at the intersections of the lines presented in Figure 1b. Figures 4 and 5 show time series of the alongshore and cross-shore momentum terms of the external mode, over the northern and southern coastal areas. The left panels show the time series of the geostrophically balanced zeroth-order terms, while the right panels show the first-order terms, including the residual of the zeroth-order balance. In fact, the terms associated with the Coriolis force and the pressure gradient are an order of magnitude larger than the remaining terms in equation (2). The residual of the difference between the geostrophic terms has the same order of magnitude as the contributions from the inertial and surface stress terms, as well as the acceleration. Although the flow tends to be primarily geostrophic, higher order terms tend to compensate the residuals of the zeroth-order balance. The largest fluctuations of the first-order terms occur in the northern region where the flow separates from the coast and becomes more prone to instability and eddy shedding (M2001). The largest oscillations between days 70 and 90, for example, coincide with the generation, development, and dissipation of a cyclonic eddy in the Gulf of Arauco (Figure 6).

[16] To clarify the role of the nonlinear terms in the dynamics of the flow, an additional numerical experiment was carried out in which we linearized the momentum equations by excluding the advective terms. Figures 6 and 7 show snapshots of the comparison between the linear and nonlinear experiments. Although the surface velocity fields in Figure 6 show a more clearly defined coastal jet in the nonlinear case, the separation of the jet from the coast at Punta Lavapie is obvious in both experiments. This agreement indicates that the separation of the jet from the coast is mostly a linear process. The offshore veering can therefore be attributed to the divergence of the isobaths at Punta Lavapie. It should be noted, however, that in the linear experiment a portion of the jet keeps flowing north along the coast, while in the nonlinear case the jet separation from the coast is complete. Another interesting result is that the formation of cyclonic eddies occurs only in the nonlinear experiment. According to our analysis the cyclonic eddies north of Punta Lavapie occur intermittently and are preceded by a relaxation of the equatorward winds, indicating that although bottom topography plays a role in the jet separation it is unimportant for eddy shedding.

[17] The zonal sections of alongshore flows in Figure 7 show that the structure of the subsurface circulation is significantly affected by the elimination of the inertial terms. In the linear case, these flows present relatively distorted vertical structures. For example, the subsurface equatorward jet attached to the slope found during our benchmark simulation (M2001) progressively disappears (or moves farther offshore) in the linear simulation. These results indicate that the nonlinear advective terms are a leading contributor to structure of the subsurface flows.

3.2. Vorticity Balance

[18] The balance equation for the vertical component of relative vorticity can be written as

$$\zeta_t = div\mathcal{J}, \tag{3}$$

where ζ_t is the rate of change (tendency) of the vertical vorticity component, and the vector field $\mathcal{J}$ is the net horizontal vorticity-flux defined as

$$\mathcal{J} = -[f\mathbf{v}] - \left[\nabla(g\eta) + \frac{1}{D}\mathbf{\Phi}\right] \times \mathbf{k} - \left[\frac{1}{D}\mathcal{A}\right] \times \mathbf{k} - \left[\frac{1}{D}\mathcal{V}\right] \times \mathbf{k}. \tag{4}$$

[19] Following the identification of terms in the horizontal momentum balance equation (2), we also identify the torque terms in equation (3) (i.e., the divergence of the four right-hand terms in equation (4)) as Coriolis, pressure gradient, horizontal advection plus diffusion (the nonlinear or inertial terms), and vertical advection plus diffusion (or surface stress plus bottom stress for the external mode). Near the surface, the vertical advection plus diffusion torque is dominated by effects of diffusion, i.e., the downward mixing of vorticity generated at the surface by the wind stress. In the external mode, the pressure torque is only due to the bottom pressure.

[20] The divergence of the flux vectors are calculated using Stoke's theorem as in the work of *Ezer and Mellor* [1994]. Notice, however, that we divide the momentum equation by the bottom depth, D, before taking the curl. The values of torque contributions are calculated using daily outputs of the model fields. The contributions of the surface stress and bottom stress torques in the external mode are separately calculated. A detailed description of equation (3) and its properties can be found in Appendix A.

[21] There are three main reasons to analyze the vorticity balance:

1. As it is directly inferred from equation (3), each flux term that can be expressed as the curl of a vectorial field (or, equivalently, each momentum term from equation (1) that can be expressed as the gradient of a potential scalar field, such as the geostrophic terms) have null contributions to vorticity changes. Thus, taking the curl of the momentum balance equation is equivalent to "filter out" the largest contributors to the flow acceleration (e.g., the geostrophic terms). This permit us to isolate and quantify the importance of the weaker momentum terms (e.g., the ageostrophic terms) in defining the flow changes. Note, then, that by "inverting" the vorticity equation, you cannot recover the total velocity field but just its ageostrophic part.

2. A consequence of the conservation property of vorticity is that we also "filter out" all type of flow changes that occur in the interior of the fluid, except those related with the transport of vorticity. So, in the vorticity fields we are observing only processes that result from the interactions of the flows with the bottom topography or with the atmosphere. This permits us to identify and

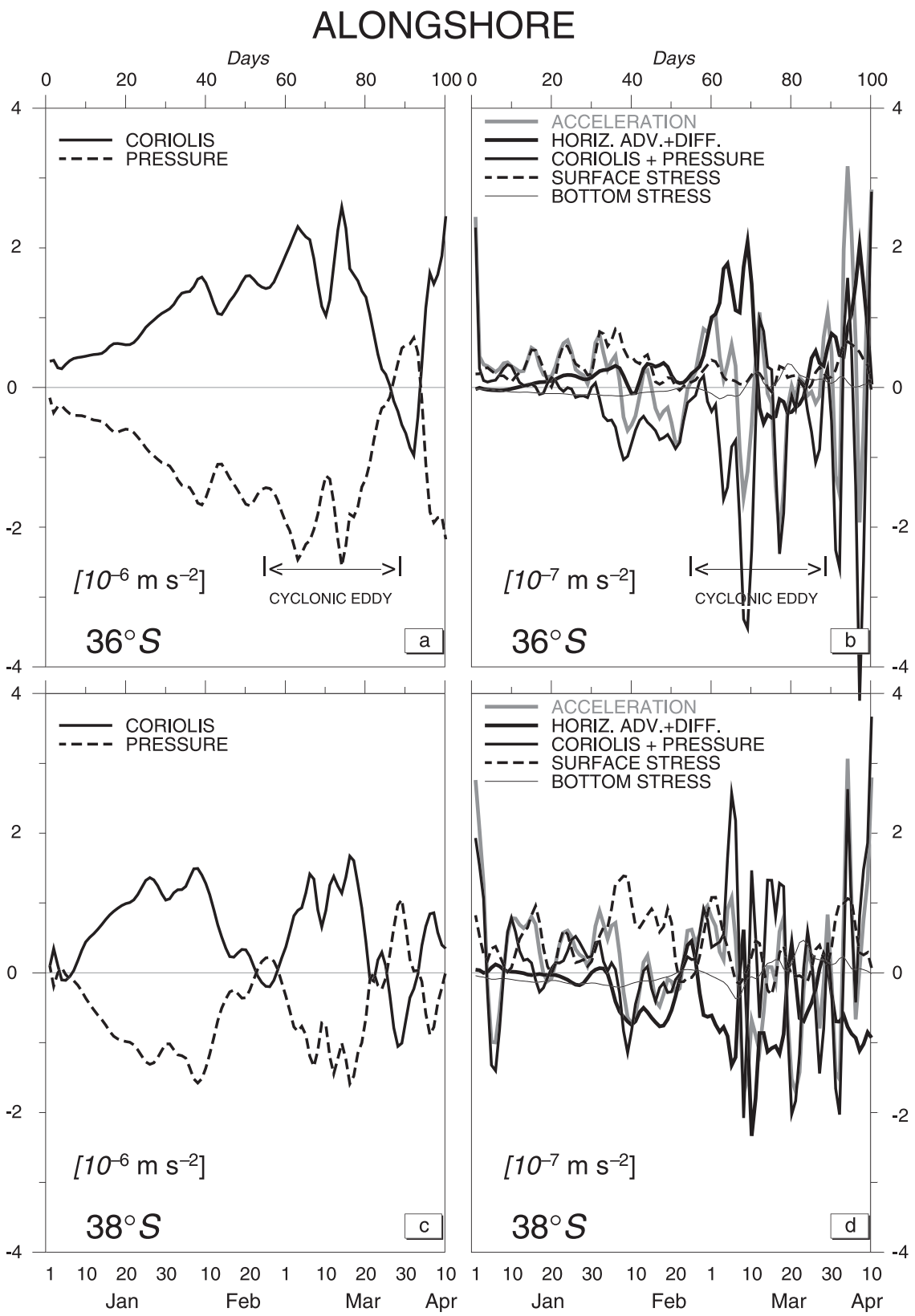

Figure 4. Upper panels show the evolution of alongshore momentum terms (external mode), representing a coastal northern region at latitude 36°S, of (a) Coriolis and bottom pressure, and (b) acceleration, inertial, surface stress, bottom stress, and the sum of the Coriolis and bottom pressure terms depicted in Figure 4a. Bottom panels show similar time series but for a southern region at latitude 38°S. Units are shown inside each panel (notice the different scales).

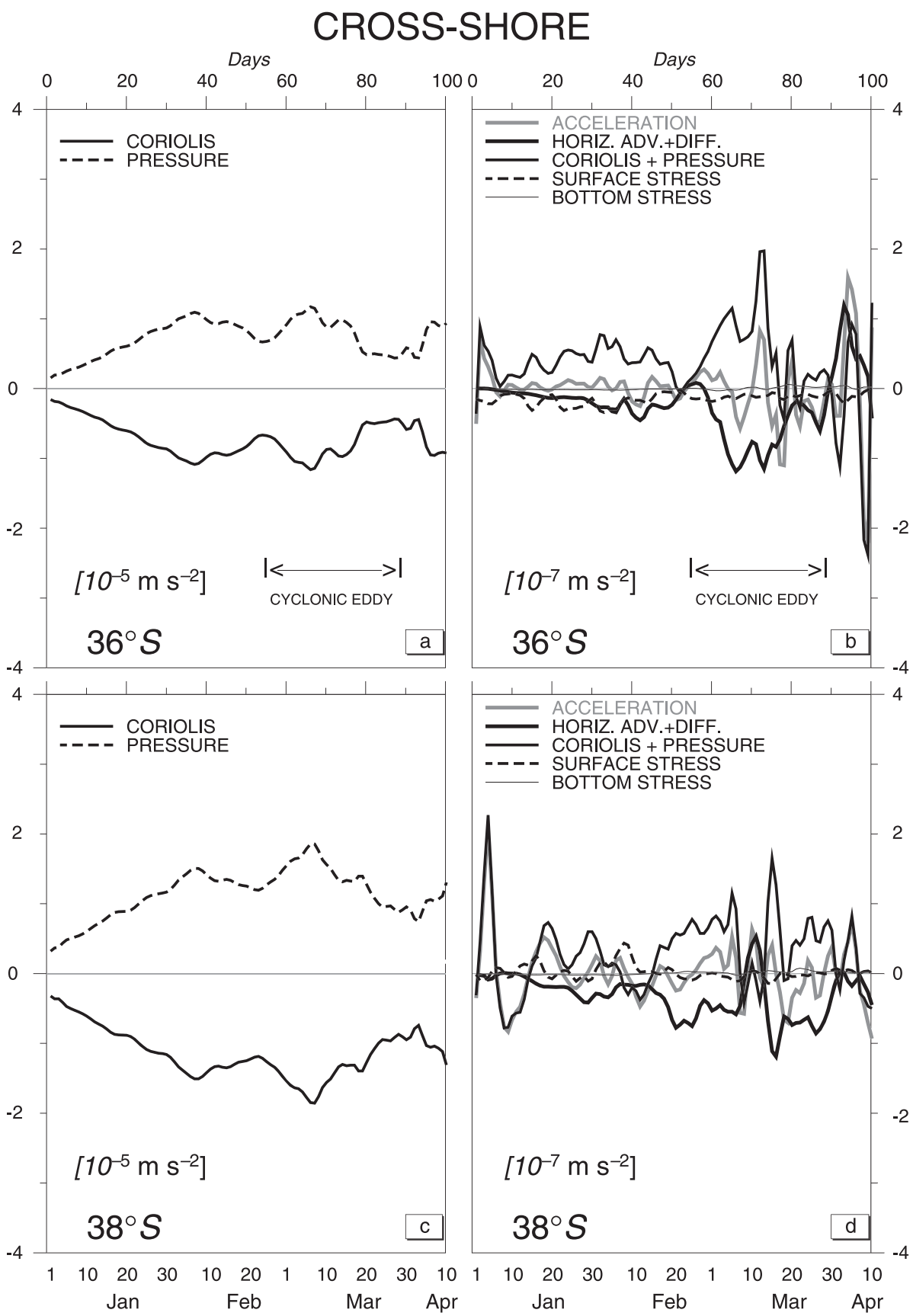

Figure 5. As in Figure 4, but for the cross-shore momentum (external mode) balances at the coastal locations.

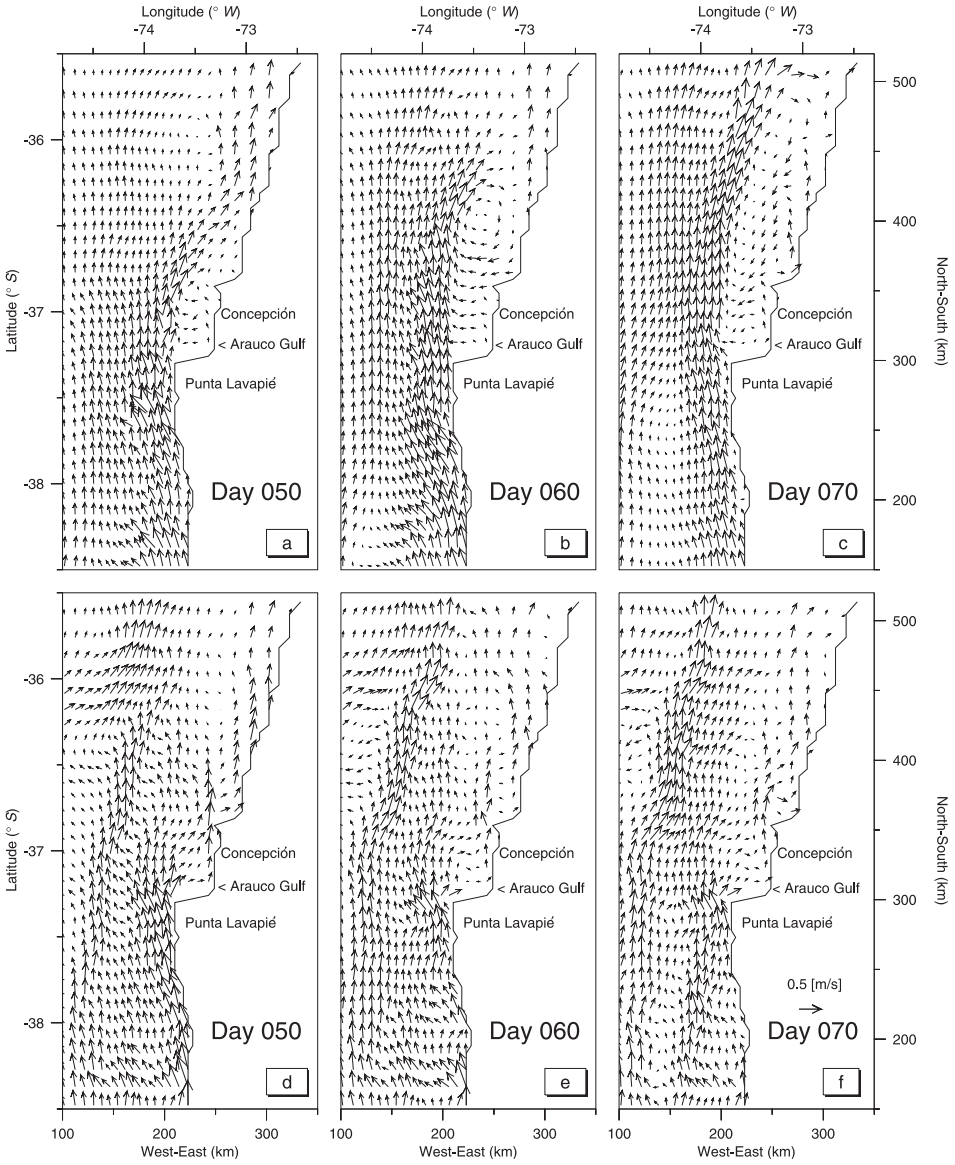

Figure 6. Snapshots of surface velocity fields at days 50, 60 and 70 for (top) the nonlinear experiment and (bottom) the simulation without the horizontal and vertical advection momentum terms.

quantify the effects of topography and coastline geometry, as well as effects of the surface wind stress, on the production or destruction of relative vorticity and on defining areas where transport of vorticity is the strongest.

3. The identification and quantification of processes of creation/destruction and transport of relative vorticity are associated to those for biochemical tracers that are important in the dynamics of an ecosystem (given that some of its components are governed by dynamic equations that are formally similar). Thus, by identifying areas of sources and sinks of vorticity we are closely identifying areas where nutrients and biomass could be accumulating or depleting.

[22] The torque components of equation (3) at each location were averaged during the last 50 days of model simulation. Table 1 shows separately the time-mean values for the external mode and for the surface part of the torque terms in equation (3), both area-averaged over the entire model domain. In agreement with the analysis of the momentum balance, Table 1 indicates that the zeroth-order vorticity balance is dominated by a quasi-equilibrium between Coriolis and the pressure gradient. The residual of these two terms is balanced by the inertial torque. The contributions from the surface and bottom stress torques to the vorticity balance are negligible.

[23] Figure 8 illustrates the spatial pattern of the time-mean zeroth-order balance for the external mode. The spatial variability of the Coriolis and bottom pressure torques between 36.5° and 39.5°S closely follow the shape of the bottom topography, particularly to cross-shore hills and canyons along the steep continental slope. Notice that contributions of the bottom pressure (Coriolis) are positive (negative) as the water flows downward over the southern walls of the cross-shore canyons, and negative (positive)

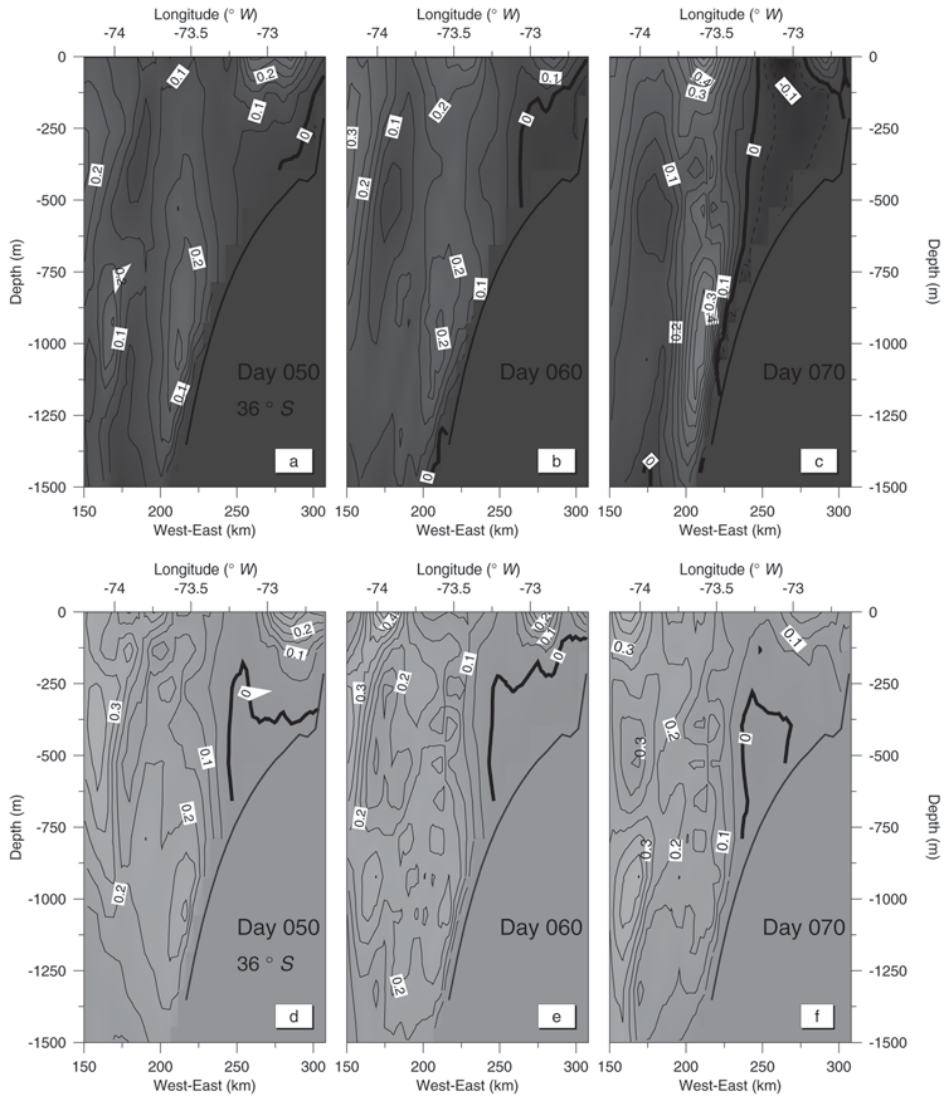

Figure 7. Zonal sections of alongshore velocity (in m s^{-1}) at latitude 36°S for days 50, 60 and 70 in (top) the nonlinear experiment and (bottom) the simulation without horizontal and vertical advection momentum terms. The contour interval is 0.05 m s^{-1} and shading denotes poleward alongshore flows.

when it flows upward over the northern walls of the cross-shore canyons (e.g., see the region between 36.4°S and 37°S). Over the upper part of the continental slope and shelf the contributions of the bottom pressure (Coriolis) show maximum (minimum) values.

[24] The spatial distribution of the residuals of the zeroth-order balance, the inertial torque, and the vorticity tendency are shown in Figure 9. Figures 9a and 9b indicate that the residual of the zeroth-order terms are balanced by the inertial terms. The location of the maxima of these terms closely follow the variations of the bottom topography, showing the influence of the bottom relief on the dynamics of the flow. The imbalances between the advection and the residual of the zeroth-order terms causes first-order changes of the vorticity tendency (Figure 9c). The spatial pattern of the vorticity tendency shows maximum values offshore of Punta Lavapie and farther north, with minimum values to the south. This spatial pattern reflects the differences in the circulation to the north and to the south of Punta Lavapie.

Table 1. Minimum, Area-Average and Maximum Values of Time-Mean Torques From the Benchmark Experiment, for the Vertically Integrated Equation (External Mode) and for the Surface (Upper 50 m) Part of the Vorticity Terms of Equation (3)[a]

	Minimum	Area-Average	Maximum
	External		
Coriolis	− 25.740	−1.124	26.100
Pressure	− 33.360	1.351	30.330
Inertia (A + D)	− 24.140	−0.084	16.470
Bottom stress	− 5.029	0.012	3.677
Surface stress	− 0.263	0.051	0.317
Tendency	− 9.723	0.206	13.970
	Surface		
Coriolis	−68.640	−1.573	116.100
Pressure	− 23.100	0.150	26.230
Horizontal A + D	−364.100	−1.037	190.500
Vertical A + D	− 23.150	4.460	27.880
Tendency	−302.200	2.000	168.500

[a]Units are $10^{-11}(s^{-2})$.

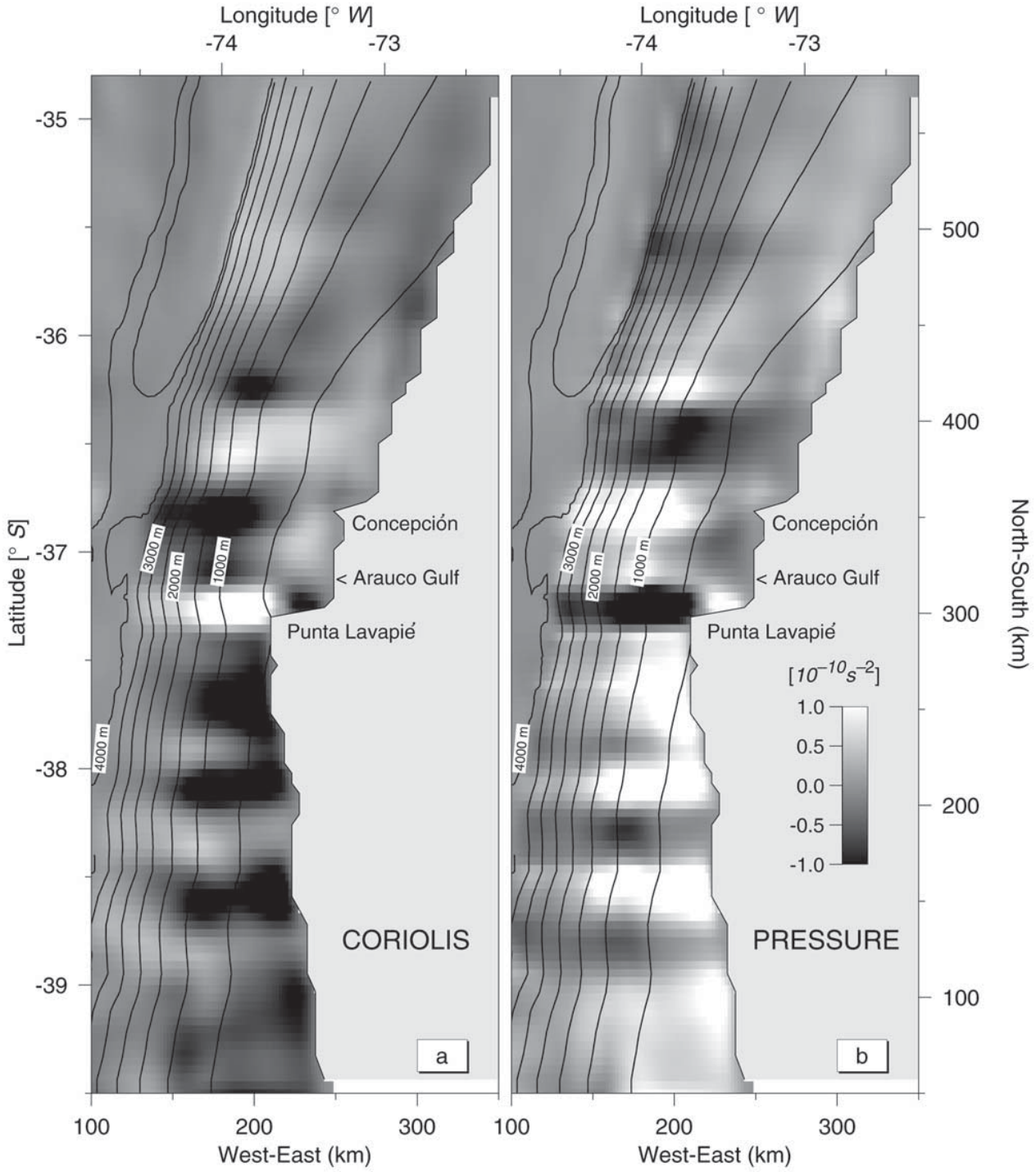

Figure 8. Maps of time-averaged external mode contributions of (a) Coriolis, and (b) bottom pressure torques, from the benchmark experiment. The white/black areas are for values larger/smaller than $\pm 10^{-10}$ s^{-2}. Overlaid are contours of bottom relief at 500-m intervals.

The circulation in the southern region is characterized by a relatively stable equatorward jet that closely follows the isobaths. North of Punta Lavapie the upwelling jet leaves the coast and turns offshore as a meandering jet shedding eddies at intermittent periods.

[25] Superimposed to the large-scale variability of the vorticity tendency there is a relatively small-scale wave-like pattern of tendency values (~10 km) (Figure 9c). These oscillations are associated with relatively large net vorticity flux vectors (Figure 9d). The close alignment of the vorticity tendency, bottom topography, and vorticity fluxes indicate that a large portion of the flow variability relates to changes in the bottom relief. The topographically induced changes are particularly strong over the slope and coastal

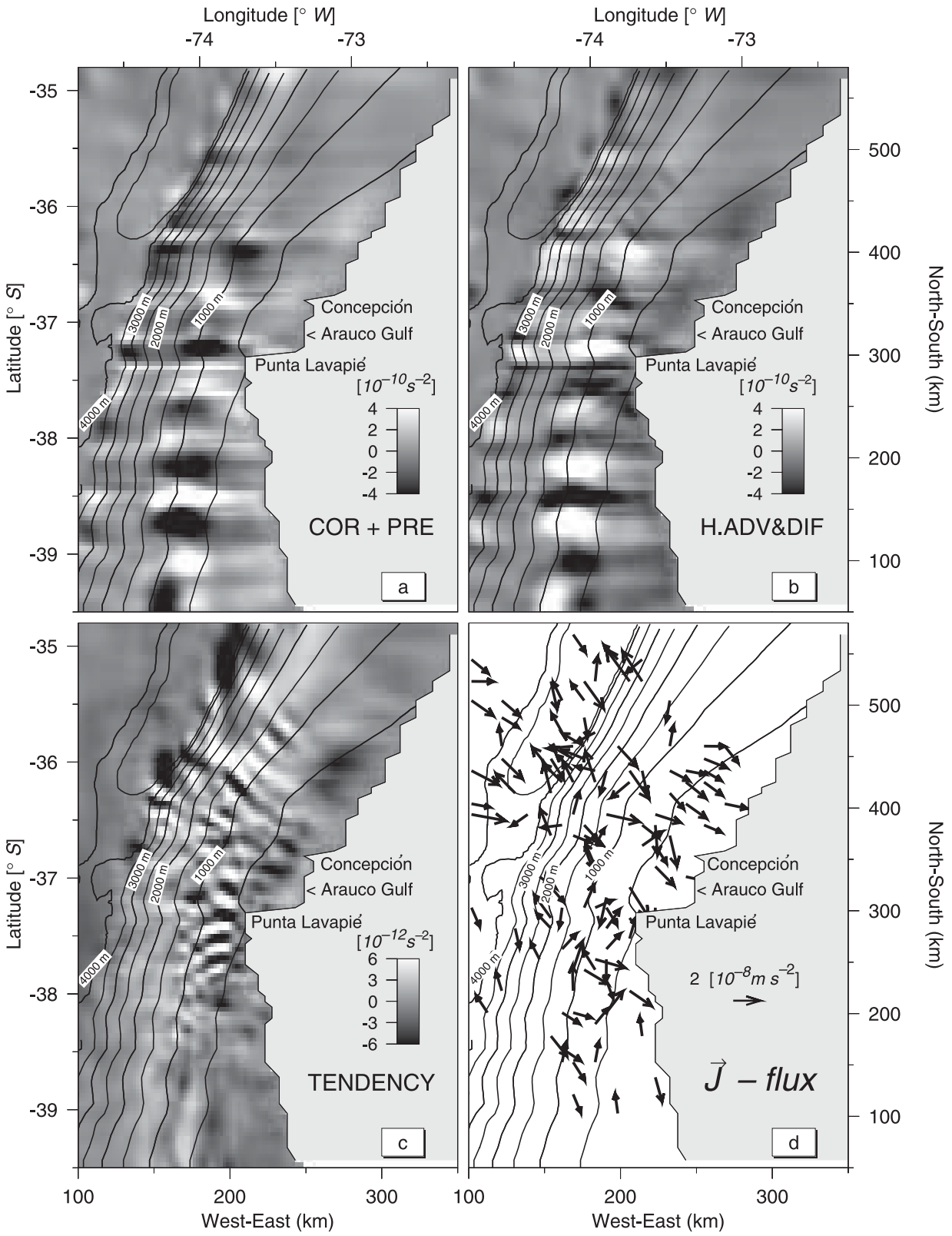

Figure 9. Maps of time-averaged external mode contributions of (a) Coriolis plus bottom pressure torques, (b) horizontal advection plus diffusion torque (inertia), and (c) vorticity tendency, from the benchmark experiment. The white/black areas are for values larger/smaller than $\pm 4 \sim 10^{-10}$ s^{-2} or $\pm 6 \sim 10^{-12}$ s^{-2}. Overlaid are contours of bottom relief at 500-m intervals. (d) The $\mathcal{J}$ vorticity flux vectors only with magnitudes larger than their area-averaged values.

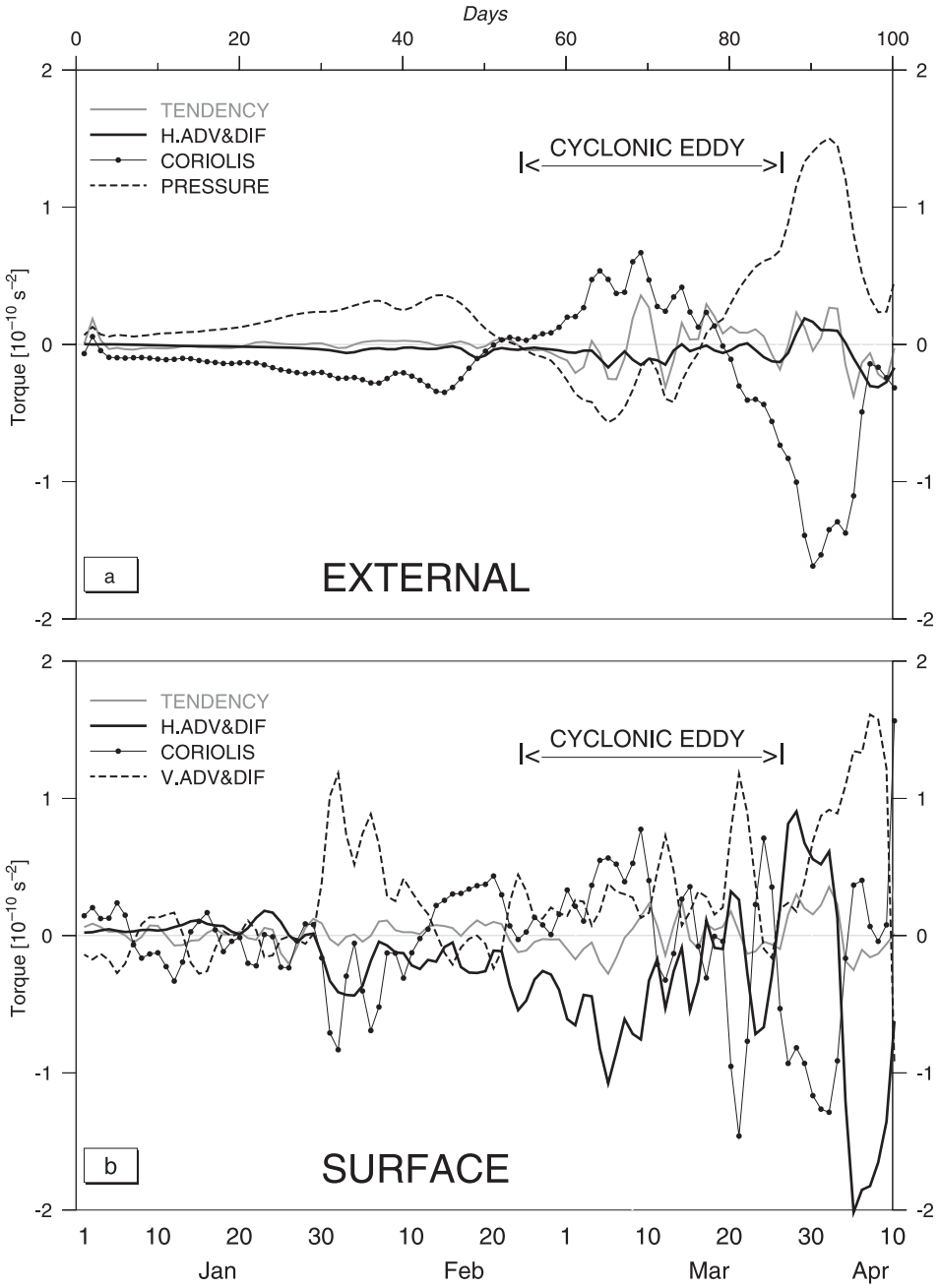

Figure 10. Evolution of the vorticity torques from a coastal northern location at 36°S. Contributions are for (a) external mode, and (b) surface part (upper 50 m) of the vorticity terms of equation (3).

areas near and north of Punta Lavapie, and on the inshore side of the Peru-Chile Trench in the north. According to the flux vectors depicted in Figure 9d, relative vorticity is created along the axes of the depth-integrated currents (due to strong interactions between the currents and the bottom topography), and then exported toward the continental coastline surrounding the Punta Lavapie cape and the interior of the Peru-Chile Trench areas, where it is dissipated.

[26] The results just discussed correspond to the analysis of the depth integrated velocity torque. As expected from theory, the vorticity balances for the surface (upper 50 m) and subsurface flows are qualitatively different (Table 1). Thus, while the subsurface flows tend to follow the planetary vorticity contours (f/D), the effects of vertical advection and diffusion (of the curl of the wind stress) are as large as Coriolis and horizontal advection in the surface layer. To illustrate these differences, in Figure 10 we show the dominant torques of the vorticity balance for the surface and subsurface (external) flows at a northern coastal location (36°S). The vorticity balance for the external mode shows a dominant balance between the torques of the Coriolis forces and the bottom pressure (Figure 10a). The vorticity balance for the surface layer shows periods of domination by the wind stress torques (vertical advection), and the inputs from the Coriolis and horizontal advection terms.

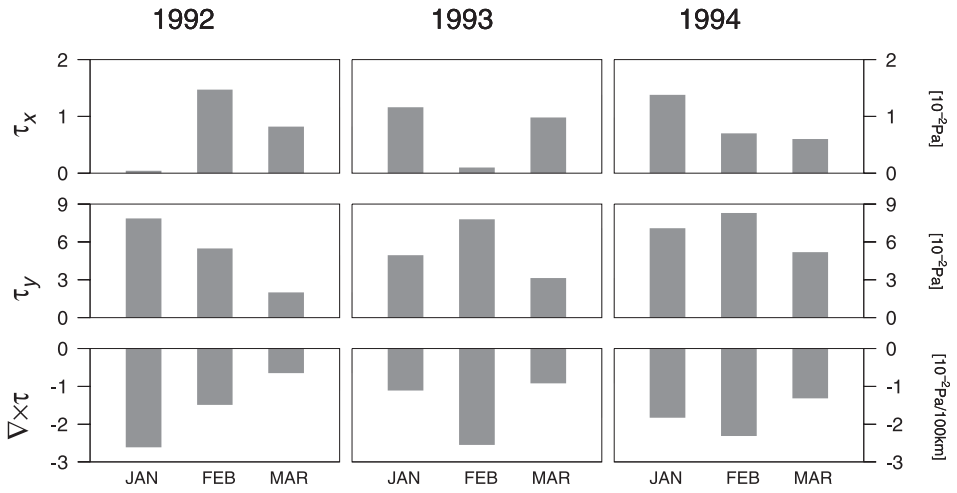

Figure 11. Monthly means of area-averaged wind stress components and wind stress curl fields for summers of 1992, 1993 and 1994. Positive values of τ_x and τ_y indicate eastward and northward winds, whereas negative values of $\nabla \times \tau$ indicate winds with cyclonic curl.

[27] Our analyses of the momentum and vorticity balances show that the topographic control is the primary cause for the separation of the jet from the coast. The nonlinear terms, in turn, play a critical role in the formation of cyclonic eddies north of Punta Lavapie, and have contributions that are strongly correlated to changes in the bottom topography. The interpretation of these correlations is that while the general tendency of the currents is to flow along planetary vorticity contours, inertial effects force the current to cross isobaths at places where their change of curvature is too abrupt for the flow to adapt. In other words, inertial effects become important where the scale of the flow is larger than the scale of the bottom topography. The sharp bending of the coastline and the rapid offshore deepening of the bottom relief that characterize Punta Lavapie identify this cape as one of such places. The imbalance between the residuals of the zeroth-order terms and the inertial contribution at those places generates a time variability of the flow.

4. Interannual Variability

[28] In this section we analyze the response of the oceanic circulation off central Chile to interannual changes in the strength of the wind stress forcing. To that end, we compare the results of two new experiments forced with winds corresponding to summers of 1992 and 1994. The along- and cross-shore components of the wind stress and the wind stress curl for these summer periods, as well as for summer of 1993, are shown in Figure 11. During 1992, there is a continuous weakening of the alongshore winds as the summer season progresses from a maximum in January to a minimum in March. A different pattern is observed in 1993 and 1994 when the strength of the alongshore winds increases from early summer to mid-summer (February), then decreases to a minimum in March as the fall season approaches. The early weakening of the upwelling favorable equatorward winds observed during 1992 is associated with a moderate El Niño event during 1991–1992. The 1992 winds become especially weak during February and March. In contrast, the equatorward winds for the same months during 1994 are stronger and highly favorable for coastal upwelling.

[29] The differences between the strength and timing of the wind patterns for El Niño and non-El Niño years reflect interannual changes of the atmospheric Subtropical Anticyclone of the Southeast Pacific (SASP) [*Ramage*, 1986]. During El Niño years (e.g., 1992) the SASP anti-cyclone weakens and reaches its southernmost extension during early summer. During non-El Niño years (e.g., 1994 or 1993) the anti-cyclone reaches its southernmost extension during mid-summer (February). Spectral calculations (not shown) indicate that the equatorward wind stress in both 1992 and 1994 are dominated by low-frequency signals with periods of 20 days or longer, and with secondary peaks in the 2- to 10-day band. The 20-day signals in 1992 were larger than in 1994, as expected between years with El Niño and non-El Niño atmospheric conditions [*Rutllant*, 1993].

[30] To illustrate the effect of the different wind patterns on the oceanic circulation, Figure 12a shows the time evolution of the basin-averaged barotropic kinetic energy from our experiments for summers of 1992 and 1994. The kinetic enaergy levels for January of 1992 are higher than those corresponding to January 1994. By mid-February, however, the relative magnitude of the energy levels is reversed to a stage where the kinetic energy levels corresponding to El Niño [1992] are less ($\sim$30–50%) than during the non-El Niño year [1994]. The differences in the kinetic energy levels (Figure 12a) for 1992 and 1994 correspond with the differences in both the strength of the wind stress fields and the surface heat flux of both years, implying that during 1992 the upwelling activity was substantially weaker than during 1994.

[31] Figure 13 shows the temporal evolution, during the summers of 1992 and 1994, of the surface density field and alongshore velocities along the coastal line illustrated in Figure 1b. The difference between the fields is presented in the bottom panels of Figure 13, where the shaded (negative)

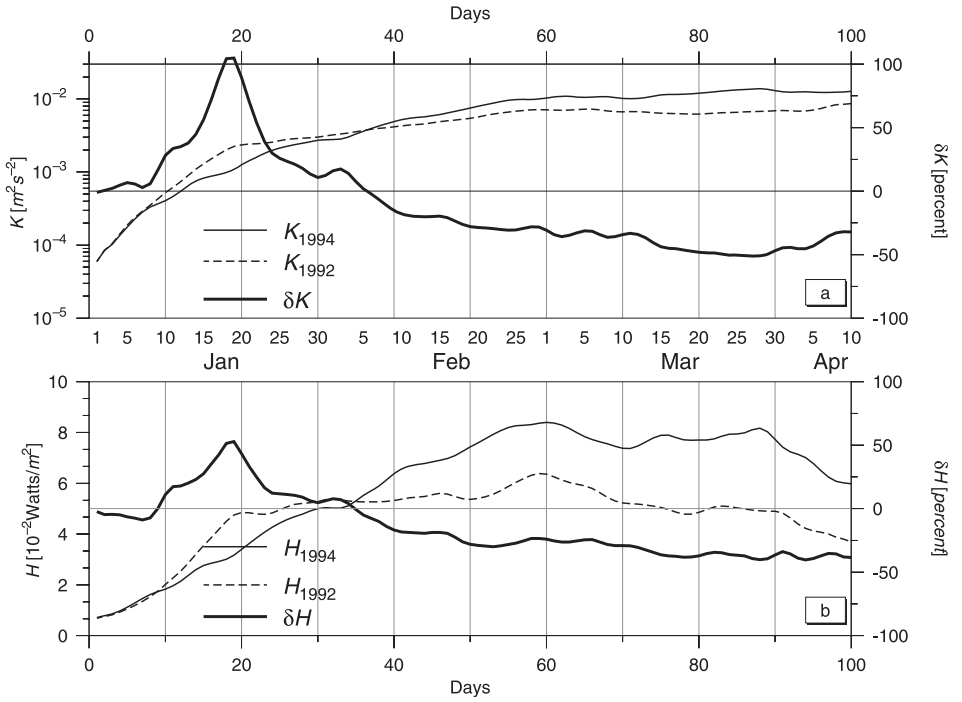

Figure 12. Evolution for summers of 1992 and 1994 of (a) volume-averaged barotropic kinetic energy (K) and (b) area-averaged surface heat energy inputs. Thick lines correspond to their differences as defined by $\delta P = 100 \times (P_{1992} - P_{1994})/P_{1994}$ (percent), where P represents the K or H fields.

areas indicate regions that in 1994 have stronger equatorward flows and denser waters than in 1992. North of Punta Lavapie, the alongshore coastal currents from 1992 and 1994 present similar levels of magnitude and of eddy shedding activity. To the south of Punta Lavapie, the equatorward currents are during 1994 persistently stronger than during 1992. North of Punta Lavapie, also, there is observed an eddy shedding process that appears as a ~20 days fluctuation of the alongshore currents (Figures 13a and 13c). To the south of Punta Lavapie, this signal is not observed. The density fields shown in Figure 13 indicate that for the last 50 days of simulation, there is more intense upwelling during 1994 than during 1992, as denser surface waters extend along the coast.

[32] The largest interannual differences between the atmospheric and the oceanic circulation of years 1992 and 1994 occur during the last 30 days (March) of the summertime period (Figures 11, 12, and 13). Figure 14 shows that during March of 1994 the upwelling activity extends farther offshore than during March of 1992. Although the surface currents of 1994 and 1992 have similar levels of magnitude (with almost zero difference in the alongshore component (Figure 13)), during 1994 they present more meanderings and have more intense cross-shore currents than during 1992. During both years the meandering activity and the separation of the jet at Punta Lavapie lead to the formation of cyclonic and anti-cyclonic eddies at both sides of the equatorward jet (e.g., the pair of cyclonic and anti-cyclonic eddies centered at ~(−73.6°W, 36°S) and ~(−73°W, 36°S), respectively, during both years).

[33] Figure 15 shows vertical sections across some of those eddies. During both years the surface eddies appear as a complex structure of equatorward and poleward surface currents. However, during years with relatively strong winds they correspond to a system of subsurface currents and countercurrents extending downward the 250 m depth, both at 36°S and 38°S. The mid-subsurface poleward currents are formed on the offshore side and upward of the predicted subsurface equatorward current located over the upper continental slope at ~1000 m depth.

[34] The separation of the equatorward jet from the coast, north of Punta Lavapie cape, is a recurrent feature that induces strong cross-shelf transport of mass, momentum and vorticity. A similar circulation pattern has been reported to occur in the eastern boundary current system off the west coast of North America. There, the separation from the coast of the equatorward upwelling jet has been observed to occur at Cape Blanco, a point of inflexion of the Oregon coast similar to Punta Lavapie [*Barth et al.*, 2000]. The main difference between the two systems is that the separation of the jet from the coast off Oregon seems to be highly influenced by a poleward undercurrent. The separation in our simulations off Chile does not appear to be a result of the poleward undercurrent but is more related to the tendency of the flow to follow isobaths and continue in a straight line as the coastline deflects to the east.

5. Summary and Conclusions

[35] In this article we analyze the momentum and vorticity balances of a numerical simulation of the upwelling regime off central Chile, and its response to interannual changes in the local wind forcing. The analyses of the momentum and vorticity balances show that the topographic control is the primary cause for the separation of the jet from the coast (at Punta Lavapie). Although the nonlinear

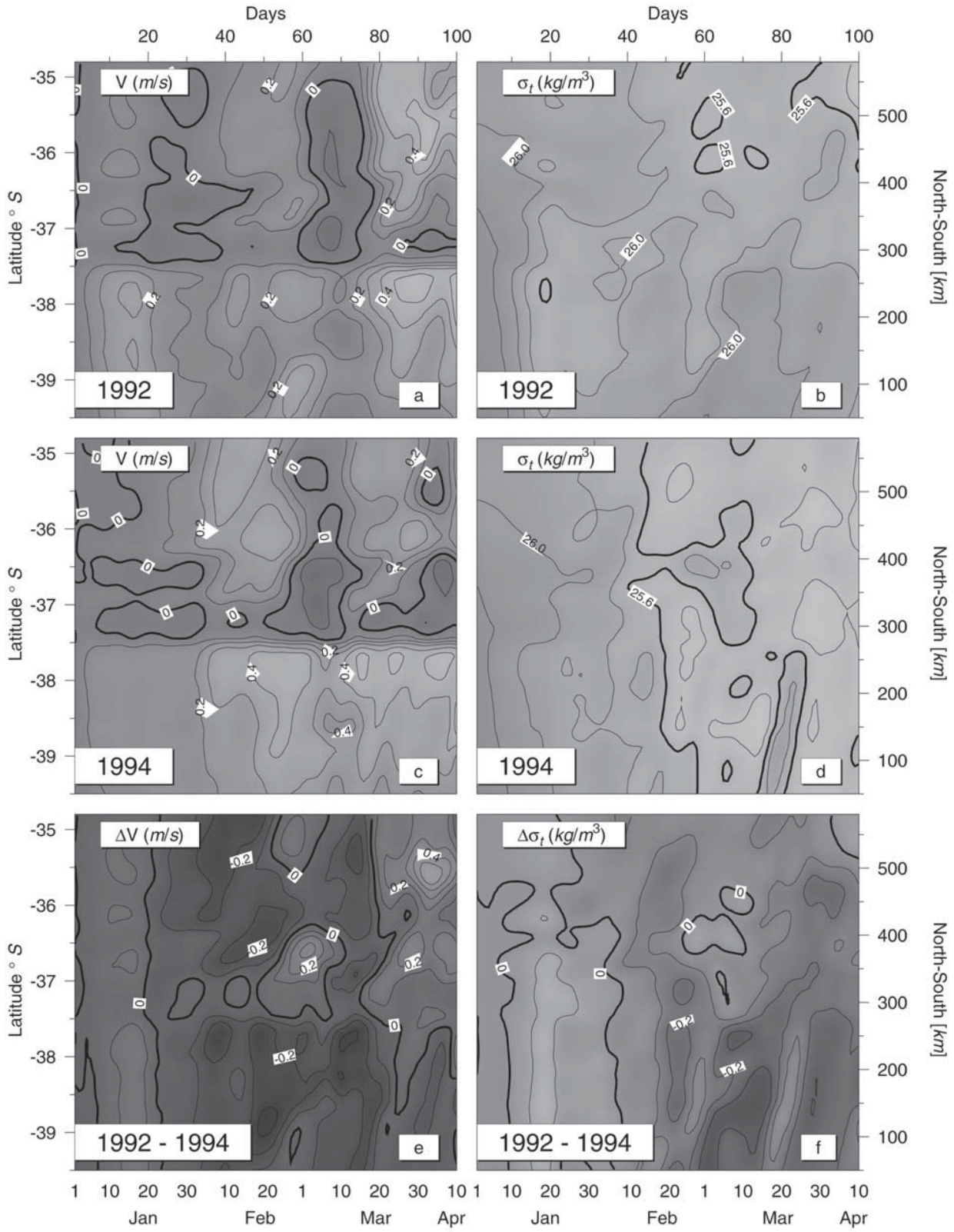

Figure 13. Evolution during summers of 1992 and 1994 of surface density and alongshore velocity from the ''coastal'' line shown in Figure 1b. Bottom panels depict the corresponding model field differences (1992–1994). Contour intervals are 0.2 kg m^{-3} and 0.1 m s^{-1}, and fields are smoothed. Shaded areas for the 1992 and 1994 years (top and middle panels) represent denser waters or southward flows. Shaded areas in their difference fields (bottom panels) with negative values represent waters or equatorward flows that in 1994 are denser or stronger than in 1992.

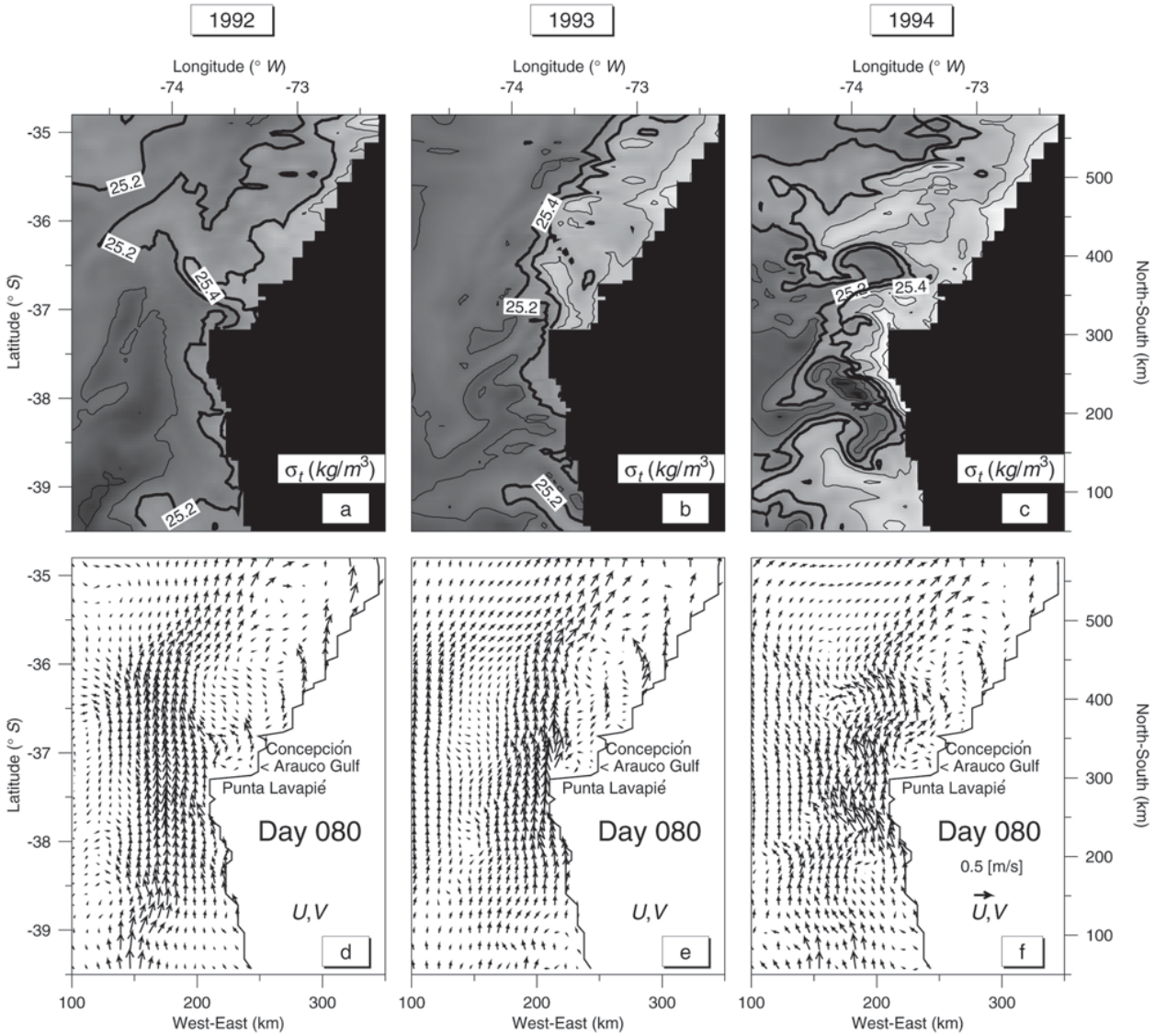

Figure 14. Snapshots of (a–c) surface density and (d–f) velocity fields for day 80 during the experiments for the summers of 1992, 1993 and 1994.

terms play a secondary role in the jet separation process, they are critical to the formation of cyclonic eddies north of Punta Lavapie. Our analyses also show that vorticity is mainly created along the axes of the subsurface currents, particularly near Punta Lavapie, and transported into the Gulf of Arauco and the Peru-Chile Trench. Our interpretation of the strong correlations between the momentum and vorticity terms and bottom topography is that while the general tendency of the currents is to flow along planetary vorticity contours, inertial effects force the current to cross isobaths at places where their change of curvature is too abrupt for the flow to adapt. This occurs at the Punta Lavapie cape, where the imbalance between the residuals of the zeroth-order terms and the inertial contribution generates a significant temporal variability of the flow.

[36] A comparison of numerical simulations aimed at investigating the effects of interannual variations indicate that years with weaker upwelling favorable wind stress forcing result in a general weakening of the upwelling system. Years with stronger wind stresses, in contrast, result in a farther offshore extension of the upwelling activity and increased across-shelf transport of mass, heat and vorticity. The changes in the strength of the wind forcing also affect the time variability of the flow, and has the greatest effect in the region north of Punta Lavapie. Thus, these results show that the Punta Lavapie cape has a large effect on the spatial and temporal variability of the coastal currents in the region off central Chile.

Appendix A: Vorticity Equation

[37] The balance equation of the vertical component of relative vorticity is given by

$$\zeta_t = \mathbf{k} \cdot curl\mathcal{F}, \tag{A1}$$

where $\zeta_t \equiv \mathbf{k} \cdot curl\left(\frac{1}{D}\frac{\partial(vD)}{\partial t}\right)$ is the rate of change of the vertical component of relative vorticity (the vorticity

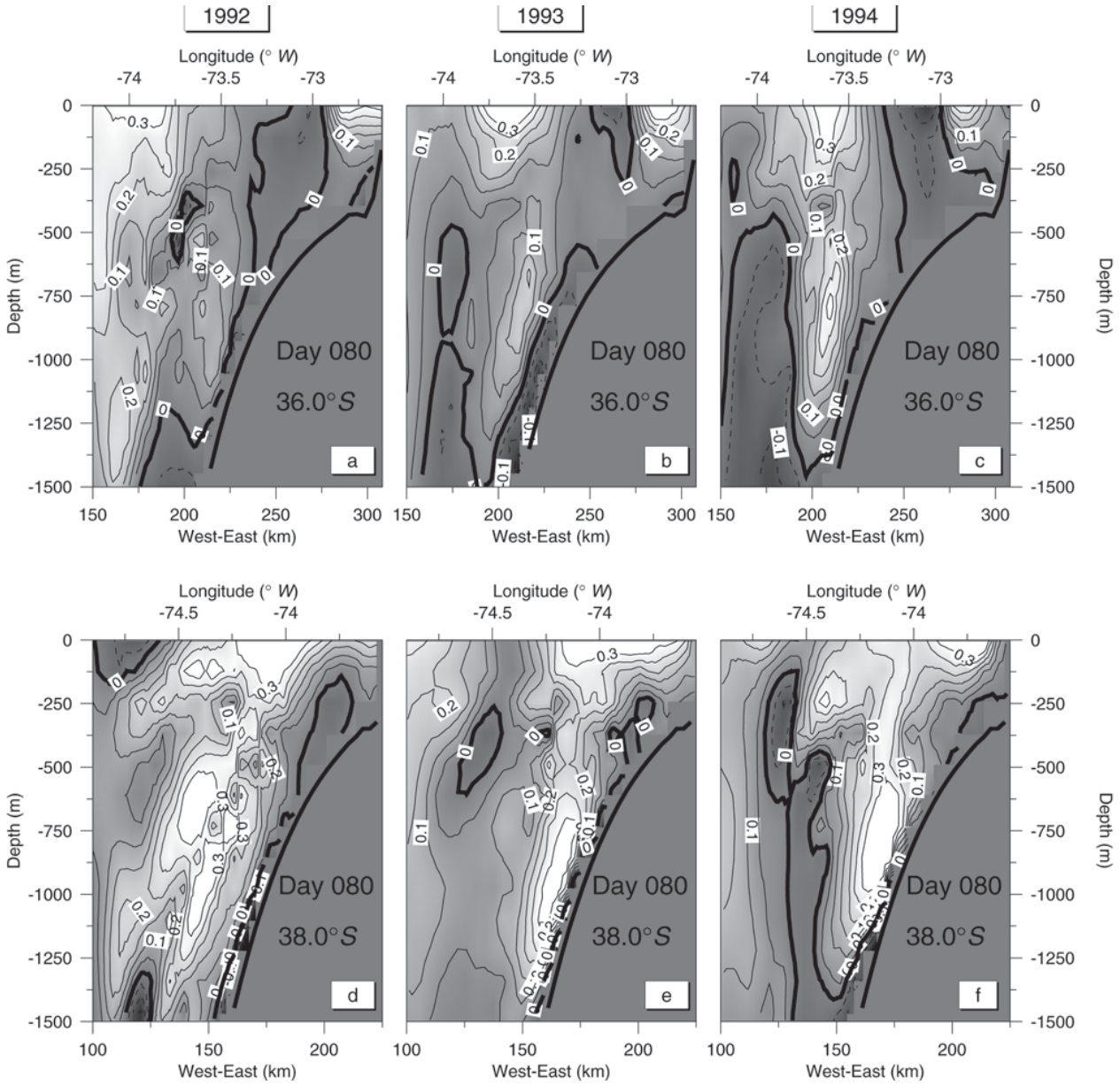

Figure 15. Zonal sections of alongshore velocity (in m s^{-1}) at latitudes 36° and 38°S and day 80 of the 1992, 1993 and 1994 experiments. The contour interval is 0.05 m s^{-1} and shading denotes poleward alongshore flows.

tendency), and $\mathcal{F}$ is given by equation (2). Since **k** is fixed, then equation (A1) can be transformed into

$$\zeta_t = div\mathcal{J}, \tag{A2}$$

with $\mathcal{J} \equiv \mathcal{F} \times \mathbf{k}$.

[38] Equation (A2) allows the classical interpretation of vertical vorticity as an Eulerian conservative variable with $\mathcal{J}$ representing the net horizontal flux or transport of vertical vorticity. Note that the partial pressure flux term $\nabla(g\eta) \times \mathbf{k}$ and the geostrophic part of the Coriolis term both have null divergences. Therefore, the contributions of the pressure plus Coriolis terms to vorticity tendency and horizontal transport are reduced to those determined by the baroclinic pressure flux $\left(\left[\frac{1}{D}\Phi\right] \times \mathbf{k}\right)$ plus the ageostrophic Coriolis term ($f\mathbf{v}_a$). The net contribution to vorticity tendency of the Coriolis term is, then, $\zeta_t^C = |f|div(\mathbf{v}_a) - \beta v_a$, the balance between the divergence and β torque of the ageostrophic flow fields. Here, $\beta \equiv \frac{\partial f}{\partial y}$ and v_a is the northward component of the ageostrophic velocity.

[39] The property of Eulerian conservation of vorticity is fully independent of the nature of the $\mathcal{F}$ field. It means that vertical vorticity cannot be destroyed or created except at fluid boundaries, which are the only regions where vorticity flux isolines can end, although in the fluid interior they can close on themselves, signaling the recirculation of vorticity. Inside of the fluid, vorticity can only be transported from one site to another. By definition, $\mathcal{J}$ -flux vectors are normal to the vertical direction, implying that horizontal surfaces are impermeable to transports of vertical vorticity.

Analogous and generalized conservation theorems for vorticity and potential vorticity can be found in the papers by *Haynes and McIntyre* [1987, 1990].

Notation

$D \equiv H + \eta$,	bottom depth;
H	bottom topography;
η	surface elevation;
$\mathbf{v} \equiv (u, v)$,	horizontal velocity;
$\mathbf{k}$	fixed vertical direction;
f	Coriolis parameter
$g \equiv 9.81\ \mathrm{m\ s^{-2}}$,	gravity constant
$\nabla \equiv \mathbf{i}\frac{\partial}{\partial x} + \mathbf{j}\frac{\partial}{\partial y}$,	horizontal gradient
σ	vertical coordinate
ω	"transformed" vertical velocity
A_M	horizontal viscosity coefficient
K_M	vertical mixing coefficient.

[40] **Acknowledgments.** Support for J. M. Mesias and P. T. Strub came from NSF grant OCE-9711344 (GLOBEC NEP) and NASA grants JPL 958128 (TOPEX) and NAG5-6604 (SeaWiFS). R. P. Matano acknowledges the support of NSF grant OCE-0118363. This is contribution 350 of the U.S. GLOBEC program, jointly funded by NSF and NOAA. The authors would like to thank the anonymous reviewers of our manuscript, whose comments helped to improve our article. J. M. Mesias also thanks James J. Bisagni and Amit Tandon, both from the School for Marine Sciences and Technology at the University of Massachusetts, Dartmouth, for kindly allowing him to finish this article.

References

Allen, J. S., P. A. Newberger, and J. Federiuk, Upwelling circulation on the Oregon continental shelf, 1, Response to idealized forcing, *J. Phys. Oceanogr.*, *25*, 1843–1866, 1995.

Barth, J. A., S. D. Pierce, and R. L. Smith, A separating coastal upwelling jet at Cape Blanco, Oregon and its connection to the California Current System, *Deep Sea Res., Part II*, *47*, 783–810, 2000.

Blumberg, A. F., and G. L. Mellor, A description of a three-dimensional coastal ocean circulation model, in *Three-Dimensional Coastal Ocean Models*, vol. 4, Coastal Estuarine Sci., edited by N. Heaps, pp. 1–16, AGU, Washington, D. C., 1987.

Ezer, T., and G. L. Mellor, Diagnostic and prognostic calculations of the North Atlantic circulation and sea level using a sigma coordinate ocean model, *J. Geophys. Res.*, *99*(C7), 14,159–14,171, 1994.

Haynes, P. H., and M. E. McIntyre, On the evolution of vorticity and potential vorticity in the presence of diabatic heating and frictional or other forces, *J. Atmos. Sci.*, *44*, 828–841, 1987.

Haynes, P. H., and M. E. McIntyre, On the conservation and impermeability theorems for potential vorticity, *J. Atmos. Sci.*, *47*, 2021–2031, 1990.

Levitus, S., and R. Gelfeld, NODC inventory of physical oceanographic profiles, *Key to Oceanogr. Rec. Doc. 18,* Natl. Oceanic Data Cent., Washington, D. C., 1992.

Lonnberg, P., D. Shaw, and P. Unden (Eds.), Research manual 1, ECMWF data assimilation, scientific documentation, Eur. Cent. for Medium-Range Weather Forecasts, Reading, England, 1989.

Mellor, G. L., and T. Yamada, Development of a turbulence closure model for geophysical fluid problems, *Rev. Geophys.*, *20*, 851–875, 1982.

Mesias, J. M., R. P. Matano, and P. T. Strub, A numerical study of the upwelling circulation off Central Chile, *J. Geophys. Res.*, *106*, 19,611–19,623, 2001.

Ramage, C. S., El Niño, *Sci. Am*, *254*, 76–83, 1986.

Rutllant, J., Coastal lows and associated southerly wind events in north-central Chile, paper presented at Fourth International Conference on Southern Hemisphere Meteorology and Oceanography, Am. Meteorol. Soc., Hobart, Australia, 1993.

Smagorinski, J., General circulation experiments with the primitive equations, I, The basic experiment, *Mon. Weather Rev.*, *91*, 99–164, 1963.

Strub, P. T., J. M. Mesias, V. Montecino, J. Rutllant, and S. Salinas, Coastal ocean circulation off western South America, in The Sea, vol. 11, edited by A. R. Robinson and K. Brink, H., pp. 273–313, John Wiley, New York, 1998.

Vergara, J., Effects of coastline geometry on wind-induced upwelling in the Chilean coast: A numerical study, paper presented at Fourth International Conference on Southern Hemisphere Meteorology and Oceanography, Am. Meteorol. Soc., Hobart, Australia, 1993.

R. Matano and T. Strub, College of Oceanic and Atmospheric Sciences, Oregon State University, Corvallis, OR 97331, USA. (rmatano@oce.orst.edu; tstrub@oce.orst.edu)

J. Mesias, School for Marine Science and Technology, University of Massachusetts Dartmouth, New Bedford, MA 02744, USA. (jmesias@umassd.edu)